

Autonomous Grid-Forming Inverter Exponential Droop Control for Improved Frequency Stability

R. W. Kenyon, *Member, IEEE*, A. Sajadi, *Senior Member, IEEE*, and B. M. Hodge, *Senior Member, IEEE*

Abstract—This paper introduces the novel *Droop-e* grid-forming power electronic converter control strategy, which establishes a non-linear, active power–frequency droop relationship based on an exponential function of the power output. A primary advantage of *Droop-e* is an increased utilization of available power headroom that directly mitigates system frequency excursions and reduces the rate of change of frequency. The motivation for *Droop-e* as compared to a linear grid-forming control is first established, and then the full controller is described, including the mirrored inversion at the origin, the linearization at a parameterized limit, and the auxiliary autonomous power sharing controller. The analytic stability of the controller, including synchronization criteria and a small signal stability analysis, is assessed. Electromagnetic transient time domain simulations of the *Droop-e* controller with full order power electronic converters and accompanying DC-side dynamics, connected in parallel with synchronous generators, are executed at a range of dispatches on a simple 3-bus system. Finally, IEEE 39-bus system simulations highlight the improved frequency stability of the system with multiple, *Droop-e* controlled grid-forming inverters.

Index Terms—power electronic converters, renewable power generation, grid-forming, frequency stability, non-linear power-to-frequency control

I. INTRODUCTION

The large-scale integration of renewable energy, driven in part by world-wide carbon emission targets, lower marginal and capital costs, and environmental and air quality benefits, is primarily achieved with power electronic converters (PECs) that integrate variable renewable energy resources (such as wind and solar photovoltaics) into the AC power grid [1], [2]. These renewable driven PECs introduce new complexities into the operation and planning of power systems at all timescales [3], while also presenting the potential to engineer particular system-level dynamic responses that were historically driven in the short-term by the physics of synchronous generators (SGs). This work introduces the novel exponential droop control (*Droop-e*) for grid-forming (GFM) PECs, leveraging their unique device level capabilities to improve the system level disturbance response of power systems of all sizes.

The increased adoption of PECs in power systems has impacted the traditional stability regimes (voltage, rotor-angle, and frequency), while necessitating the introduction of two more (resonance and converter-driven) [4]; this work focuses on frequency stability at the inertial and primary response

time frames and the improvements possible with novel PEC controllers. It is well established that large penetrations of grid-following (GFL) PECs, the predominant contemporary type that explicitly require an exogenous reference phasor for operation, can lead to frequency instability [5], while even grid-supporting mechanisms of these GFLs at high penetrations have been observed as insufficient to mitigate instabilities [6]. As a result, there has been substantial interest in the integration of GFM inverters that regulate the local voltage phasor and directly control the device frequency response [7]. Substantial research and experimentation has shown that these devices improve frequency stability in conjunction with SGs [8], [9], while also providing substantial benefit to the frequency response of power systems via increased damping [10]. However, at high shares of GFM devices with the most common linear droop control, the rate of change of frequency (ROCOF) is exacerbated and high frequency oscillations with other SGs can occur [11].

A review of the state-of-the-art reveals that a variety of control schemes exist for the GFM approach [12]–[14], including static (i.e., linear) droop [15], virtual synchronous machine [16], [17], and virtual oscillator control [18]. Variations on linear droop include feed-forward mechanisms, virtual impedance loops for reactive power sharing, and adaptive droop with a power differentials [19]. The general concept of frequency shaping is presented in [20]. Matching control adjusts the device frequency based on the DC-link capacitor voltage state [21]. Varied linear droop values are explored briefly in [22]. The work in [23] explored the concept of an exponential type droop control for reactive power sharing in resistive networks. Zhong [24] investigates limitations in droop control based on resistive impedances. GFM power limiting with proportional-integral driven frequency reductions were presented in [22] and [25].

The novel, non-linear, power to frequency *Droop-e* control provides multifaceted improvements including: 1) a larger utilization of available headroom, 2) a less deviant nadir and a more favorable rate of change of frequency (ROCOF), 3) improved frequency dynamics with a higher damping capability, and 4) a natural power limiting behavior. An auxiliary controller leverages the GFM direct frequency control to achieve autonomous power sharing amongst interconnected devices within the primary frequency response time frame. The *Droop-e* control strategy represents immense potential for improving the frequency stability and resilience of emerging power grids by utilizing available energy resources more efficiently, especially battery energy storage systems (BESS) that are typically not operating near power limits [26].

The authors are with the Renewable and Sustainable Energy Institute (RASEI) at the University of Colorado Boulder.

Dr. Hodge and Dr. Kenyon are with the Electrical, Computer, and Energy Engineering department at the University of Colorado Boulder.

Dr. Hodge and Dr. Sajadi are with the National Renewable Energy Laboratory in Golden, Colorado.

An elementary version of the exponential control has been presented by the authors in [11] and shown to improve the frequency stability of a Maui power system model following a generation loss in [27]. This paper presents the fully developed *Droop-e* controller accompanied by a full analytic stability assessment and a host of simulations depicting the range of possible operations. The remainder of the paper proceeds with a discussion on non-linear control motivation in Section II, a full controller description in Section III, analytical stability assessments in Section IV, and electromagnetic transient simulations on a simple 3-bus and the IEEE 39-bus system in Section V-B. The presented control design, analysis, and simulation results firmly establish the capability of the *Droop-e* control to improve the frequency stability of power systems at any penetration of PECs.

II. MOTIVATION FOR NON-LINEAR FREQUENCY CONTROL

This section summarizes the fundamental device frequency response of SGs and droop controlled GFM that were rigorously analyzed in [11], highlighting the contrasts that serve as the motivational basis for the novel *Droop-e* control.

A. Linear Droop

Following a transient load-generation imbalance, the SG first follows an inertial response, wherein the angular frequency ($d\delta_G/dt = \omega_G$) changes according to the swing equation (1):

$$\frac{2H}{\omega_s} \frac{d^2\delta_G}{dt^2} = p_m - p_e - D\left(\frac{d\delta_G}{dt} - \omega_s\right) \quad (1)$$

where δ_G is the generalized rotor angle, H is the device inertia constant, ω_s is the synchronous frequency, p_m is the rotational mechanical power, p_e is the electrical power delivered to the network, and D is the damping component. As ω_G changes, the governor and turbine adjust p_m during the primary response, which is broadly described by (2):

$$T_{TG} \frac{dp_m}{dt} = -p_m + p_{set} - \frac{1}{M_D} \left(\frac{\omega_G}{\omega_{set}} - 1 \right) \quad (2)$$

where p_{set} is an exogenous active power setpoint, M_D is the droop gain (i.e. 5% in the United States), ω_{set} is the frequency setpoint, T_{TG} is the turbine-governor time constant, and ω_G is the SG frequency. The inertial response period represents an uncontrolled exchange of rotational energy with the connected network. Comparatively, the controlled primary response of an SG is a reaction to a change in frequency. The amount by which p_m changes is a control design; smaller M_D values yield larger p_m changes. Instability due to the increase in rate of change of p_m occurs with small M_D values [11]. Setting $M_D = 0$ is mathematically, and therefore physically, infeasible.

The linear droop GFM frequency dynamics are shown in (3) and (4):

$$\frac{d\delta_I}{dt} = M_D (p_{set} - p) + \omega_{set} \quad (3)$$

$$\frac{d\omega_I}{dt} = -M_D \omega_{fil} (p - p_{meas}) \quad (4)$$

where δ_I is the inverter electric angle, p_{set} is the exogenous power setpoint, p is the filtered active power, ω_I is the inverter frequency, ω_{fil} is the power measurement cutoff frequency, and p_{meas} is the measured, instantaneous power output. ω_I is not a control variable in the frequency dynamics of the GFM. Within the inertial and primary response periods, the frequency changes only after a change in power is registered; these are proactive devices. The value $M_D \omega_{fil}$ is congruent with the inverse of mechanical inertia ($1/H$); here it is considered an ‘effective inertia’ as it represents the rate of change of frequency for this control type. Smaller M_D values yield a greater effective inertia and therefore M_D is a lever to influence both the change, and rate of change, of frequency.

B. Concept of Droop-e

The primary idea behind the *Droop-e* concept is supplanting the linear droop frequency control of a GFM device (3) with an exponential function of power dispatch:

$$\frac{d\delta_I}{dt} = D_e(p, p_{set}) \quad (5)$$

where D_e is the yet to be presented (in the preceding section) *Droop-e* control. This approach allows a design wherein the change in frequency can be reduced for devices with large headroom, allowing them to exchange larger active power magnitudes with a network with corresponding smaller frequency deviations. This is accomplished by using p as the independent variable in an exponential function. An exponential function is chosen instead of a power or quadratic because the tangent value does not go to zero when the argument is zero as with the others, a characteristic that has been shown to lead to instability in [11]. An added benefit of the *Droop-e* control is that the inertial response of the GFM, i.e., the resistance to a change in frequency with a change in power, is directly impacted by the tangent value of the exponential function at a particular operating point:

$$\frac{d\omega_I}{dt} \propto \frac{\partial}{\partial p} D_e(p, p_{set}) \quad (6)$$

where \propto is the proportional operator. The result is that because the *Droop-e* control enables a larger use of headroom, this simultaneously improves the frequency stability of the system with a larger effective inertia. Additionally, near the power limits, the exponential curve is yielding an increased change in frequency with respect to power, incurring a natural device level limiting. The ability of the GFM device to deliver this active power rests on the assumption of an appropriately designed DC-link with the primary energy source and associated controller tuning. The work in [11] has shown with rigorous simulation that with a sufficient design, this assumption of available active power is suitable for frequency control.

III. THE DROOP-E CONTROLLER

This section establishes the core mathematics and rationale behind the *Droop-e* controller, and accompanying secondary power sharing controller, with the block diagram shown in Fig. 1. The expression for *Droop-e* control with the individual frequency components is Eq. (7):

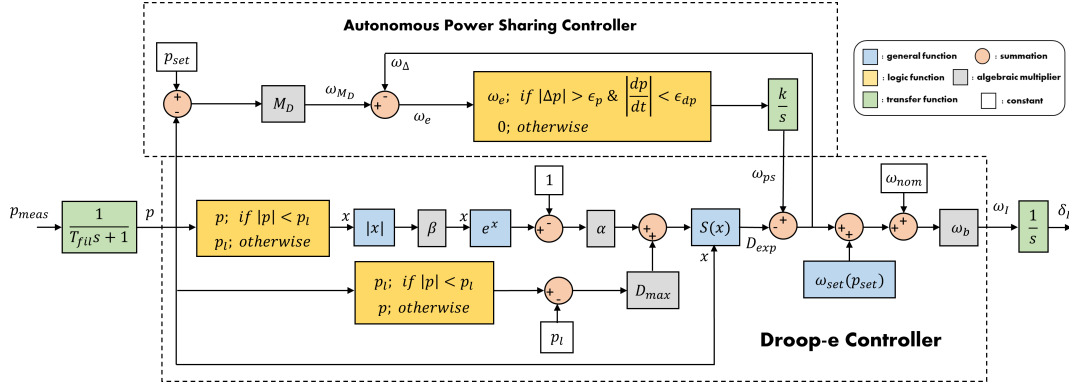


Fig. 1: The full *Droop-e* controller that receives the filter output power p , and calculates the output frequency ω_I . The autonomous power sharing controller adds a frequency offset ω_{ps} to achieve power sharing within the primary frequency response period, only if this control objective is desired. The calculation of p_l and ω_{set} are not explicitly shown.

$$D_e(p, p_{set}) = \omega_b [\omega_{nom} + \omega_{set}(p_{set}) + D_{exp}(p) + \omega_{ps}] \quad (7)$$

where ω_{nom} represents the nominal frequency setpoint, $\omega_{set}(p_{set})$ is the non-linear frequency offset, $D_{exp}(p)$ is the core exponential sliding mode frequency response, and ω_{ps} is the post transient autonomous power sharing component, all in per unit; ω_b is the base frequency of the system. The term $\omega_{set}(p_{set})$ is required to add an additional frequency offset due to the non-linear droop characteristics of the $D_{exp}(p)$ term. This section proceeds by addressing the exponential shaping in III-A, the inversion at the origin in III-B, limiting the maximum droop value in III-C, and handling the frequency setpoint in III-D. Section III-E presents the autonomous power sharing controller that adjusts the term ω_{ps} in Eq. 7 after a transient. The *Droop-e* controller is parameterized with specific values in III-F, and accompanying curve traces are presented.

A. Shaping the Exponential Curve

Considering first an active power argument domain of $p \in [0.0, 1.0]$, the core exponential $E(p)$, as a function of p is:

$$E(p) = -\alpha e^{\beta p} \quad (8)$$

where α and β are the linear and argument scalars, respectively. There is a negative sign explicitly in (8) because the slope must always be negative for synchronization in an AC network [20]. α is selected to yield smaller droop values at lower dispatches, and β is selected to drive a rapid increase in droop values near the dispatch limits. The first power derivative of $E(p)$ is:

$$\frac{dE(p)}{dp} = -\alpha\beta e^{\beta p} \quad (9)$$

which expresses the ‘tangent droop value’ at the operating point p . At low power dispatches, the $E(p)$ is primarily driven by the product $\alpha\beta$. To maximize headroom delivery at lower dispatches, while bounding the minimum droop value for stability, the following relationship is established:

$$M_{min} \leq \alpha\beta < M_D \quad (10)$$

where D_{min} is a minimum droop value parameter.

B. Inverting the Curve

To maintain the synchronization criteria, the curve must be mirrored and inverted at the origin ($p = 0$). This inversion capability is constructed for an argument domain of $x \in [-1.0, 1.0]$, which represents the active power output of a battery energy storage system. An analogous result is obtained for devices capable of only a positive power export ($p \in [0, 1.0]$), with a projection $p_{control} = 2p - 1$, where $p_{control}$ is used in the *Droop-e* formulation, and the inversion occurs at $p = 0.5$. All subsequent controller expressions are cast with p only. The absolute value function ($|x|$) is defined as in (11):

$$|x| := \begin{cases} x, & \text{if } x \geq 0 \\ -x, & \text{if } x < 0 \end{cases} \quad (11)$$

The function $S(x)$ is defined as $S(x) := 2H(x) - 1$, where $H(x)$ is the Heaviside function ($H(x) = 1$ if $x \geq 0$, $= 0$ otherwise). The output characteristic of $S(x)$ is (12):

$$S(x) = \begin{cases} 1, & \text{if } x \geq 0 \\ -1, & \text{if } x < 0 \end{cases} \quad (12)$$

With the $|x|$ and $S(x)$ functions, the formulation in (13) achieves an inverted reflection at the origin.

$$E_I(p) = -S(p) \left[\alpha \left(e^{\beta|p|} - 1 \right) \right] \quad (13)$$

C. Limiting the Droop Value

Without limiting, the tangent droop value at maximum magnitude power outputs can be large and may be an undesirable operating characteristic. This is addressed by introducing a maximum droop value parameter, D_{max} . This is equal to the tangent droop value of E_I at a particular operating power, defined as p_l . The power outputs at which D_{max} occurs are at equal magnitude; i.e., $-p_l$ and p_l , due to the symmetry about the origin of (13). When operating past this p_l value, the control reverts to linear droop as in (3), where $M_D = D_{max}$. The expression in (14) captures the inversion at the origin and the linearization for power outputs beyond p_l :

$$D_{exp}(p) = \begin{cases} -S(p) [\alpha (e^{\beta|p|} - 1)], & \text{if } |p| < p_l \\ -S(p) [\alpha (e^{\beta p_l} - 1) + D_{max}\Delta p], & \text{otherwise} \end{cases} \quad (14)$$

where $\Delta p = |p| - p_l$. The tangent droop value of E_I is equal to D_{max} when $|p| = p_l$. The derivative of E_I with respect to p is shown in (15):

$$\frac{\partial E_I}{\partial p} = -\alpha\beta e^{\beta|p|} \quad (15)$$

With (15) set equal to D_{max} , p_l is calculated as:

$$p_l = \frac{\ln\left(\frac{D_{max}}{\alpha\beta}\right)}{\beta} \quad (16)$$

with the negative sign dropped due to the origin symmetry.

D. Handling the Frequency Setpoint

The non-linearity of $D_{exp}(p)$, and the linearization component, demand special attention to calculate the frequency setpoint (ω_{set}) as a function of the power setpoint (p_{set}). Equation (17) shows the case specific per unit frequency calculation, that handles these complexities of $D_{exp}(p)$.

$$\omega_{set}(p_{set}) = \begin{cases} S(p_{set}) [\alpha (e^{\beta|p_{set}|} - 1)], & \text{if } |p_{set}| < p_l \\ S(p_{set}) [\alpha (e^{\beta p_l} - 1) + D_{max}\Delta p_{set}], & \text{otherwise} \end{cases} \quad (17)$$

where $\Delta p_{set} = |p_{set}| - p_l$. For p_{set} values with a magnitude less than p_l , the frequency value along the exponential curve is calculated and added as an offset for the frequency setpoint. For p_{set} values larger than p_l , the linearization handling is captured in a similar manner. Note that the frequency setpoint is only necessary to calculate the correct setpoint at a specific power setpoint, it has no impact on the dynamic response of the *Droop-e* control.

E. Autonomous Power Sharing Controller

By design, the *Droop-e* control deviates from transient power sharing in the inertial and primary frequency response periods. The autonomous power sharing controller, shown in Fig. 1, operates by adding the offset component ω_{ps} to achieve equitable power sharing after the transient. With an offset instead of a full-bypass, the *Droop-e* control continues to provide damping to the system with $D_{exp}(p)$, but the added offset ω_{ps} changes ω_I and causes frequency responsive devices on the network to react. This power sharing controller is presented as a method to achieve autonomous power sharing within the primary frequency response period. However, this controller can be easily bypassed if automatic governor control methods are preferred in the secondary response period.

The frequency deviation that would result with a linear droop is calculated with the relation (3), ignoring the frequency setpoint (18):

$$\omega_{M_D} = (p_{set} - p)M_D \quad (18)$$

This frequency is compared with D_{exp} and the current power sharing component ω_{ps} to generate an error, ω_e :

$$\omega_e = \omega_{M_D} + D_{exp} - \omega_{ps} \quad (19)$$

This error is passed through a logic block only after a disturbance is registered, and the transients have diminished:

$$\omega_{e,out} = \begin{cases} \omega_e, & \text{if } |\Delta p| > \epsilon_p \wedge \left|\frac{dp}{dt}\right| < \epsilon_{dp} \\ 0, & \text{otherwise} \end{cases} \quad (20)$$

where ϵ_p and ϵ_{dp} are disturbance tolerance parameters. Once the disturbance criteria are met, this error is passed through an integrator block with gain k , which generates the frequency offset, ω_{ps} . As this offset is added to the output frequency ω_I , the GFM power output will change due to the dynamics of AC power transfer, causing following changes in ω_{D_e} . The GFM will arrive at the power sharing value as specified by M_D as ω_e is driven to 0 by the integrator.

TABLE I: Selected *Droop-e* Parameters

Parameter	Value
α	0.0012
β	3.2
D_{min}	0.25%
D_{max}	6.0%
ω_b	376.98 radians (60 Hz)
p_l	0.86 pu
$\min D_e = \alpha\beta$	0.45%
M_D	5%
k	0.2
ϵ_p	0.01
ϵ_{dp}	0.001

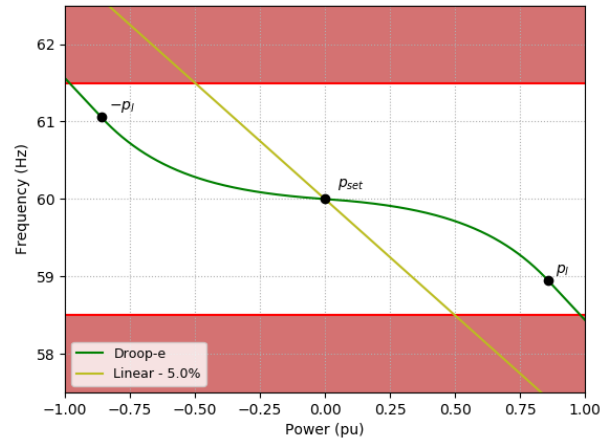


Fig. 2: *Droop-e* frequency curve as a function of power output for the parameters specified in Table I, compared to a 5% linear droop.

F. Full *Droop-e* Expression

Table I shows the *Droop-e* parameter values used for this study, which were selected to achieve a full active power output range from -1.0 to 1.0 within a frequency range of 61.5 to 58.5 Hz. Here, a D_{max} of 6% was selected to allow a natural power limiting near the peak outputs. The power-frequency curve of the *Droop-e* control with these parameters at a power dispatch of $p_{set} = 0.0$ is shown in Fig. 2. It is

evident that the Droop- e curve has the mirrored inversion at the origin, and the linearization when $|p| > p_l$.

Figure 3 shows the tangent droop value as a function p of the Droop- e curve from Fig. 2. This tangent droop is inversely proportional to the effective inertia per (9). Clearly, the Droop- e control provides a larger effective inertia to the system for the majority of dispatch points as compared to the linear 5% droop. As indicated, the droop value is limited to 6% through the linearization of the controller at values greater than $\pm p_l$.

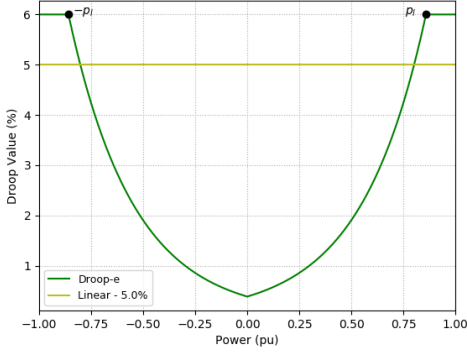


Fig. 3: Droop- e tangent droop value across the full range of power output p with parameters from Table I. Note the limits for $|p| > p_l$ and the continuous value across the range of outputs.

IV. ANALYTICAL STABILITY ASSESSMENT OF Droop- e

This section presents the analytical stability analyses of the Droop- e controller.

A. Synchronization Criteria

The power derivative of the Droop- e controller D_e across the full power output domain $p \in [-1.0, 1.0]$ is:

$$\frac{\partial D_{exp}}{\partial p} = \begin{cases} -\alpha\beta e^{\beta|p|}, & \text{if } |p| < p_l \\ -D_{max}, & \text{otherwise} \end{cases} \quad (21)$$

The derivative of D_{exp} exists at all points on the power output domain. Furthermore, because p_l is strictly defined as the power output where (15) is equal to D_{max} , the derivative is continuous at all points across the output domain. Therefore, Droop- e is continuous and smooth across the entire output domain, indicating that there are no discontinuities in the control response. The expression in (21) proves that the droop value is negative across the entire power output domain. This is a necessary criteria for synchronization in AC networks that have intrinsic, natural droop characteristics [10]; i.e., an increase/decrease in power output causes a decrease/increase in device frequency. Therefore, across the entire power output domain, the frequency is monotonically decreasing and has guaranteed stability in inductive AC networks [20].

B. Stability of the Power Sharing Controller

The autonomous power sharing controller is a closed-loop feedback control system with the control objective to add a frequency offset (ω_{ps}) to ω_I to achieve a parameterized

power sharing droop value, M_D . This process achieves equitable power sharing among all frequency response-supporting generators in the system, and is activated only after primary frequency oscillations are dissipated and its value has reached an equilibrium. The transfer function that describes this control process is given by:

$$\Delta\omega(s) = \frac{D_{exp}(p)s + kM_D\Delta p}{s + k} \quad (22)$$

where $\Delta\omega = \omega_I - \omega_{set}$ and $\Delta p = p_{set} - p$. The limit of (22) is considered for two cases. First, the limit as $s \rightarrow \infty$, which is the case for GFM power output transients (23):

$$\lim_{s \rightarrow \infty} \Delta\omega(s) = D_{exp}(p) \quad (23)$$

This limit shows that during transients, which may occur after the autonomous power sharing controller is initiated, core exponential relation remains dominate. The limit of $s \rightarrow 0$ is shown in (24):

$$\lim_{s \rightarrow 0} \Delta\omega(s) = M_D\Delta p \quad (24)$$

which indicates that the integrator in the autonomous power sharing controller will enforce the added frequency offset and achieve a change in frequency commensurate with the desired, equitable droop value, M_D .

C. Small Signal Stability Analysis

Small signal stability analysis (SSSA) is a linearization technique that is applied to a differential-algebraic equation set of a system with m differential states (x_m) and n algebraic variables (y_n) [28]. This system is linearized in the form of:

$$\Delta\dot{x}_m = A_{sys}\Delta x_m \quad (25)$$

where A_{sys} is the system state matrix that contains the algebraic variables. The complex eigenvalues of A_{sys} are $\lambda_m = \alpha_m + j\omega_m$, which capture the time-evolution of the system (25). Positive real parts ($\alpha_i > 0$) represent fundamental instability. The damping component (ζ_m) of each eigenvalue is calculated as $\zeta_m = \frac{-\alpha_m}{\sqrt{\alpha_m^2 + \omega_m^2}}$.

$$\begin{aligned} x_{SG} &= [\delta_G, \omega_G, E'_q, E'_d, E'_{fd}, V_R, R_f, p_{m,G}, p_{SV}]^T \\ x_{GFM} &= [\delta_I, p_I]^T \end{aligned} \quad (26)$$

A simple 3-bus network (shown in Fig. 5) is used for this SSSA (and subsequently in the simulations). A 100-MVA SG is located at bus 1. A battery backed ($p \in [-1.0, 1.0]$), Droop- e controlled, 50-MVA GFM PEC is at bus 3. The reactances $X_a = X_b = 0.05pu$ represent the interconnecting lines. The network bases are $S_b = 100MVA$ and $V_b = 18kV$. The load at bus 2 is constant power ($P_2 = 75MW$, $Q_2 = 25Mvar$). The SG model used is the base model from [28], represented by the block diagram of Fig. 6. The saturation function is an exponential of the form: $S_E(E_{fd}) = \gamma e^{\epsilon E_{fd}}$. Flux decay is included. The states of the 9th order model are (26). The parameters are from the 9-bus model SG 3 in [28], with governor and turbine parameters from [25].

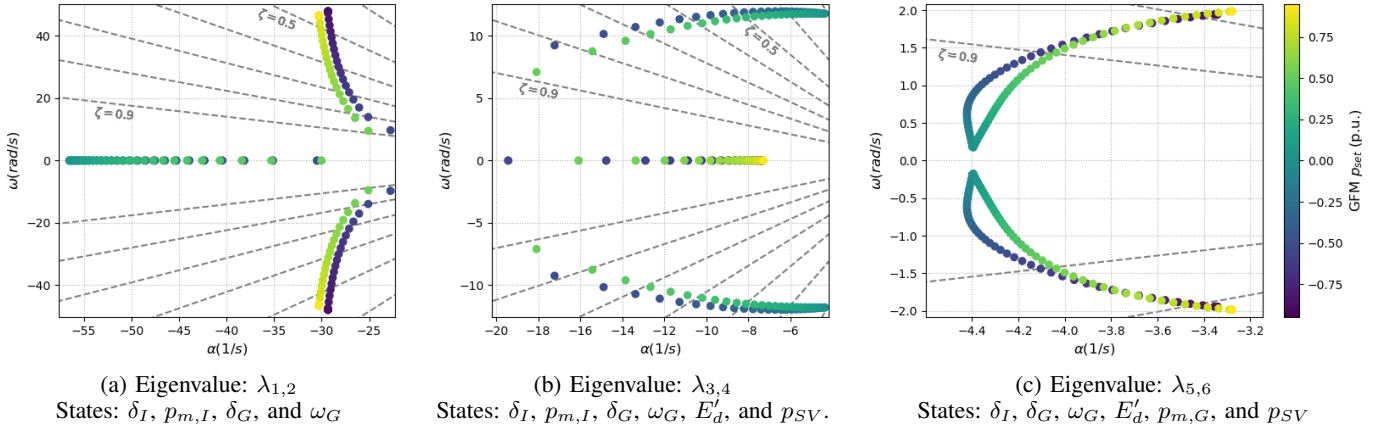


Fig. 4: Eigenvalue trajectories of the simple 3-bus system for those with GFM state participation. Note the varied x and y axis scales.

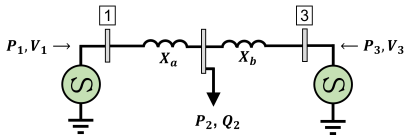


Fig. 5: The simple 3-bus system with a synchronous generator located at bus 1 and a *Droop-e* grid-forming PEC at bus 3.

The dynamic model of the GFM is as shown in Fig. 1. This model has two states, shown in (26), where the subscript I has been added. A voltage behind impedance model, with the output impedance of the LCL filter, is the circuit coupling the dynamic model to the network [25]. The internal voltage and current controllers are not modeled, and a constant voltage at the LCL capacitor is assumed [29]. It is recognized that the internal controllers can impact small signal stability [30], [31], but these oscillatory modes are outside of the scope of this study, which is focused on the slower mode SG interactions; regardless, the accompanying electromagnetic transient simulations were executed with full order GFM models. The linearization process is executed as in [28]. All network details are provided in Table V.

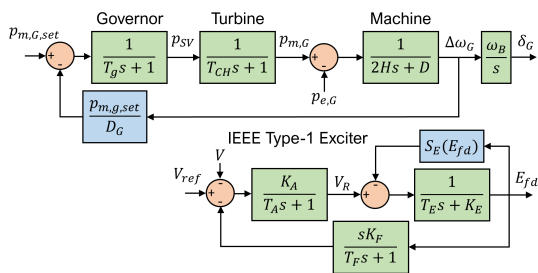


Fig. 6: The synchronous generator model with governor, turbine, machine, and exciter dynamic sub-systems.

D. SSSA Results

The eigenvalues of the 3-bus system of Fig. 5 were calculated for at the full per unit dispatch range of the battery backed, *Droop-e* controlled GFM inverter. Three complex

eigenvalue pairs were identified via participation factor analysis as involving the GFM states of; $\lambda_{1,2}$, $\lambda_{3,4}$, and $\lambda_{5,6}$. The eigenvalue pair $\lambda_{1,2}$ involves the states δ_I , $p_{m,I}$, δ_G , and ω_G . Figure 4a shows that the eigenvalue trajectory is pure real and negative, for the range $p_{set} = [-0.4, 0.4]$, and at $p_{set} = \pm 0.4$ a bifurcation occurs where modes transition from pure real to oscillatory. The damping decreases monotonically up to the full dispatch point, $p_{set} = \pm 1.0$, below $\zeta = 0.45$. Figure 4b shows the evolution of eigenvalue pair $\lambda_{3,4}$ in the left half plane, which includes participation from the states δ_I , $p_{m,I}$, δ_G , ω_G , E'_d , and p_{SV} . This eigenvalue pair has an oscillatory element at low p_{set} values that becomes increasingly damped as the dispatch magnitude increases. The mode becomes pure real at the same bifurcation point as $\lambda_{1,2}$, indicating a coupling between $\lambda_{1,2}$ and $\lambda_{3,4}$. As both modes are higher frequency and contain participation from $p_{m,I}$, but not the SG mechanical power ($p_{m,G}$), these eigenvalues driven primarily by the first-order low-pass power filter measurement of the GFM device.

The final eigenvalue pair with GFM state participation is $\lambda_{5,6}$ shown in Fig. 4c. This eigenvalue pair includes both the GFM and SG angles, and the $p_{m,G}$, and it is a low frequency mode at $0.06 \rightarrow 0.63$ Hz. The trajectory of this pair corroborates the frequency damping benefit to the system of the *Droop-e* control, particularly at low power dispatches [11]. This mode depicts a strongly damped oscillatory mode at all dispatches, with a decreasing damping as the dispatch of the GFM inverter is increased. All three eigenvalues with participation from the *Droop-e* controlled GFM device display appropriate damping, indicating that the controller is stable when connected in parallel with a SG device across the range of possible dispatches.

V. ELECTROMAGNETIC TRANSIENT SIMULATIONS

This section details the electromagnetic transient dynamic simulation experiments conducted on the simple 3-bus, and the IEEE 39-bus test systems to assess the time-domain response of the *Droop-e* control in a variety of operating conditions. These simulations were conducted in the PSCAD software package [32]. The GFM PEC is represented with a core 13th-order model including internal current and voltage controllers,

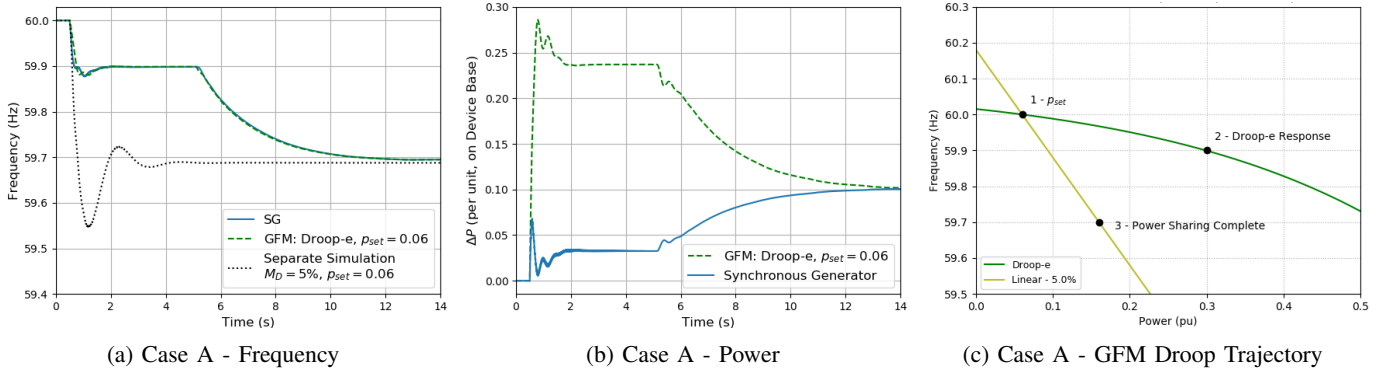


Fig. 7: The frequency response, power response, and droop trajectory for the GFM and SG devices in Case A.

an output LCL filter, and power filtering. A 4th order battery energy storage system model is accompanied by a 2nd order buck-boost controller to regulate the DC-link voltage of the core PEC model. The GFM device is executing a reactive power-voltage droop control ($Q - V$). A full description of the models and networks can be found in references [29] and [11]. The SG model was constructed with internal PSCAD models. The device network parameters are in Appendix VII, Table V. All models and networks are available open-source at [33]. In all cases, the simulations are executed by first bringing the system into steady state prior to releasing all dynamic elements and applying the perturbation.

The frequency nadir, and peak ROCOF, which is calculated with a sliding window of $T_w = 0.1s$; $max|f_G(t)| = \frac{\omega_G(t+T_w) - \omega_G(t)}{2\pi T_w}$, are used to characterize the system response. The frequency statistics are calculated from the SG rotational frequency alone for the 3-bus results. On the 39-bus system, the weighted average frequency is used for statistics - $f(t) = \frac{\sum_{i=1}^n (MVA_i * f_i(t))}{\sum_{i=1}^n MVA_i}$ where $f_i(t)$ is the frequency of device i at time t , MVA_i is the device i rating, and n is the number of devices. The mechanical inertia rating of the system configuration, presented in Table IV, is a weighted average calculated as $H = \frac{\sum_{i=1}^n H_i S_{B,i}}{\sum_{i=1}^n S_{B,i}}$ where H_i is the inertia rating (in s) of device i , $S_{B,i}$ is the MVA rating of device i , and n is the number of devices. $H_i = 0$ for GFM devices. The primary mode frequency and damping were calculated with the matrix pencil method [34].

A. 3-Bus System

The 3-bus system topology is identical to Fig. 5. Three simulations with $\pm 20\%$ load perturbations were executed to capture the full diversity of the *Droop-e* control. Case ‘A’ captures a load increase case for a near-zero dispatch of the GFM and case ‘B’ a load increase for a highly dispatched GFM. Case ‘C’ is a load decrease for a positive, near-zero dispatch, capturing the inversion of the *Droop-e* curve through the origin. The dispatch conditions and applied load step are summarized in Table II.

The results of case A are shown in Fig. 7, with frequency statistics in Table III. The frequency plot shows a highly damped ($\zeta = 0.17$) response of the slow frequency mode ($\lambda_{5,6}$), with a ROCOF of 0.77 Hz/s and a nadir of 59.9 Hz.

TABLE II: Dispatches for each case on a 100 MVA base.

Case	SG		Droop-e GFM		Load Step ΔS
	P (pu)	Q (pu)	P (pu)	Q (pu)	
A	0.73	0.21	0.03	0.07	20%
B	0.40	0.24	0.40	0.03	20%
C	0.73	0.21	0.03	0.07	-20%

TABLE III: Case Results—All apply prior to power sharing ($\approx 5s$); frequency statistics apply to synchronous generator shaft speed; ΔP is on 100 MVA base.

Case	ΔP_{SG} (pu)	ΔP_{GFM} (pu)	Nadir (Hz)	ROCOF (Hz/s)	Damping (ζ)
A	0.033	0.119	59.9	0.77	0.47
B	0.106	0.045	59.52	1.48	0.36
C	-0.024	-0.127	60.09 (Over Frequency)	0.68	0.52

At approximately 5 seconds, the autonomous power sharing controller engages after sensing the disturbance and a return to steady state, which moves both devices to a 5% equitable power sharing point. The results of a 5% linear droop control are shown for comparison; the *Droop-e* control yields a superior frequency response. The device powers (Fig. 7b) show that the majority of the load perturbation was met by the GFM inverter, which provides a large effective inertia at the low dispatch of $p_{set} = 0.06$. Fig. 7c shows the position on the *Droop-e* curve at p_{set} (point 1), the change in frequency with power along the *Droop-e* curve following the perturbation (point 2), and finally the position of the device on the 5% power sharing curve after the autonomous controller action is complete.

Case B, with results in Fig. 8, has a p_{set} of 0.8. There is a larger frequency deviation (Fig. 8a) as compared to case A, because the device is operating much closer to the power maximum. The ROCOF is larger, at 1.48 Hz/s, which is expected due to smaller effective inertia at the higher dispatch. The low frequency oscillatory element has decreased damping ($\zeta = 0.36$), as expected from the $\lambda_{5,6}$ power dispatch trajectory (Fig. 4c). The power outputs in Fig. 8b show that the SG delivers a larger amount of power, only because the frequency has a larger deviation from the nominal. The movement on the *Droop-e* curve in Fig. 8c shows that at this dispatch, the control moves past the linearization point (p_l), at which point a linear 6% droop is applied. This is

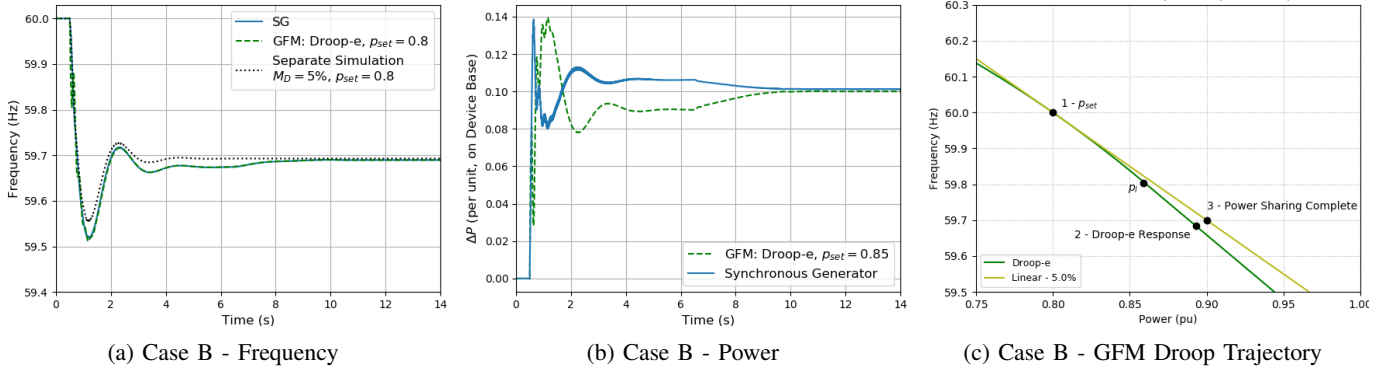


Fig. 8: The frequency response, power response, and droop trajectory for the GFM and SG devices in Case B.

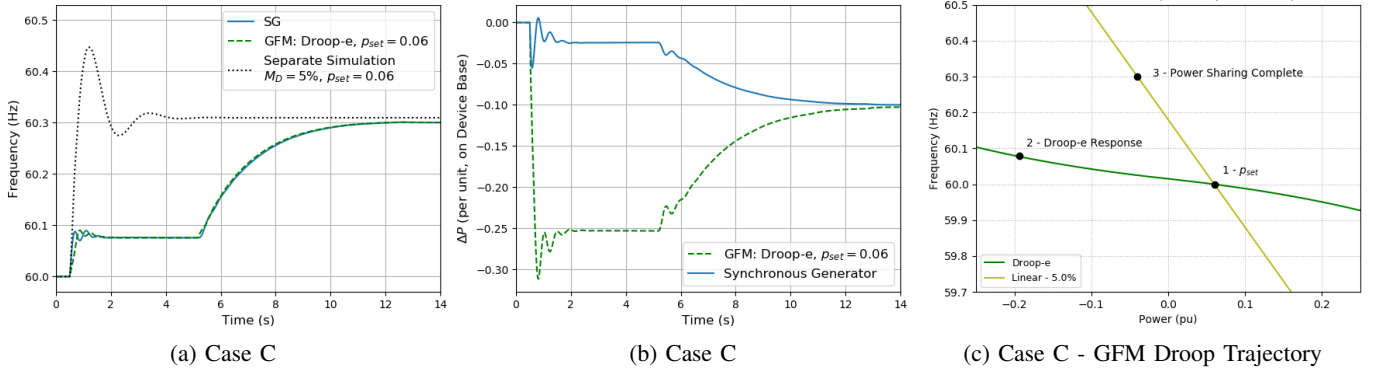


Fig. 9: The frequency response, power response, and droop trajectory for the GFM and SG devices in Case C.

corroborated by the lower frequency as compared to the 5% control simulation, and the decrease power delivery. However, this proves that the linearization control works and limits the output of the device.

The impact of a 20% load decrease at a dispatch of $p_{set} = 0.06$ for case C is shown in Fig. 9. This represents an over-frequency event, and highlights the stability of the *Droop-e* controller in a transition from a positive to a negative power output. The frequency response in Fig. 9a shows a very small increase in frequency (0.09 Hz) with excellent damping (0.52), prior to the autonomous power sharing controller action. Because the *Droop-e* curve is passing through the origin, which is the power output with the largest effective inertia, the smaller ROCOF of 0.68 as compared to case A is expected. The GFM sinks the majority of the surplus power (Fig. 9b), while the movement on the *Droop-e* curve shows the expected response (Fig. 9c), prior to achieving equitable power sharing with operation in over frequency domains. These three time-domain simulations show the successful operation of the *Droop-e* controller at critical points, the linearization near the power limits and the inversion at the origin, as well as the superiority of this GFM control method.

B. IEEE 39-Bus System

Simulations on the IEEE 39-bus test system [35] demonstrate the capability of the *Droop-e* control with multiple GFM devices. All devices are rated at 1000 MVA. The same dynamic SG model from the 3-bus simulations were used, with

the rating changed. The dispatch of the devices is shown in Fig. VI. Note that Gen 0 is operating at full output. Three cases were developed; (i) *Case 39-A* in which all generators were SGs, (ii) *39-B* where three of the generators, 0, 4, and 8, were replaced with GFMs with a linear-5% droop control, and (iii) *Case 39-C* where those three generators, 0, 4, and 8, were replaced with GFMs with *Droop-e* control. In all three cases, the dispatch of the devices remained identical, which are summarized in Table VI. The perturbation applied is a disconnection of generator 7.

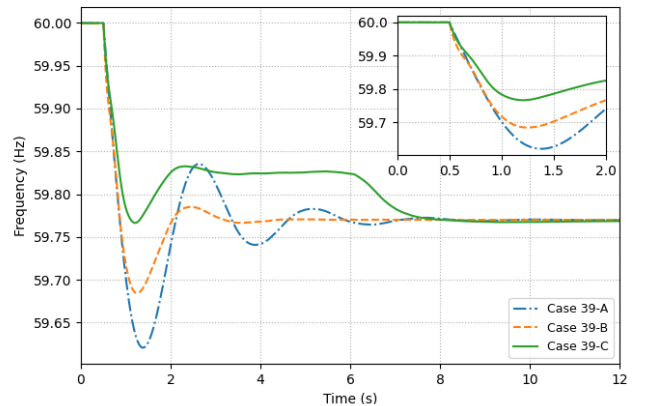


Fig. 10: Average frequency response of IEEE 39-bus system for the three cases simulated following the loss of generator 7

Fig. 10 shows the average frequency response of the system for the loss of generator 7 for each of the three cases studied.

TABLE IV: Case Results–Frequency Statistics Derived From Average

Case	Inertia (s)	Nadir (Hz)	ROCOF (Hz/s)	Damping (ζ)	Dom. Mode Freq. (Hz)
39-A	3.0	59.62	0.66	0.10	0.40
39-B	2.1	59.68	0.87	0.15	0.43
39-C	2.1	59.77	0.66	0.16	0.44

Corresponding frequency metrics are presented in Table IV. The frequency response in Case 39-A is a classic second-order response of an SG dominated power system; the nadir (59.62 Hz) was substantially lower than the settling frequency (59.77 Hz), and an inter-area oscillatory mode at 0.44 Hz is present. In Case 39-B, the frequency response is improved relative to Case 39-A. The nadir is raised to 59.68 Hz, but the ROCOF is higher at 0.87 Hz/s as compared to 0.66 Hz/s for Case 39-A, which is expected according to [11]. The frequency response with three *Droop-e* GFM devices on the system in Case 39-C is the best of all three cases. The nadir (59.77 Hz) is equal to the settling frequency, which occurs because the *Droop-e* equipped GFM devices deliver more power to the system during the initial transient, arresting the frequency decline faster than the linear droop control. However, the ROCOF is also the same as the SG-only case at 0.66 Hz/s, which occurs because of the improved effective inertia of the *Droop-e* control at these dispatches.

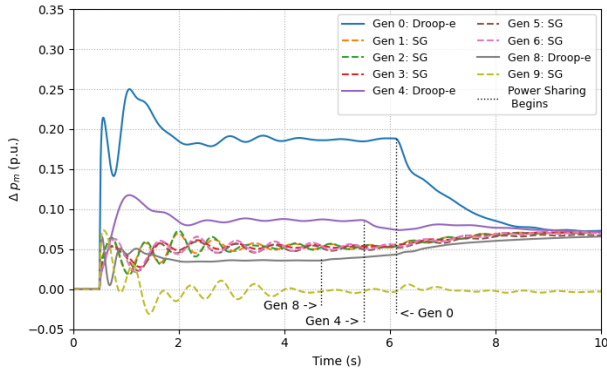


Fig. 11: Per unit active power deviations following the loss of generator 7 on the 39-bus system, case 39-C; the initiation time for power sharing of each *Droop-e* generator is highlighted.

Fig. 11 displays the power outputs of all of the generators in Case 39-C. Clearly, the *Droop-e* controlled GFM devices release more power immediately following the disturbance (coinciding with when the additional power is needed the most) and, as a result, provide more robust support to the grid during the transient period. This observation highlights the control benefit of leveraging the available headroom that is not deployed with a linear droop control; generator 0 delivered almost 3 times as much power to the network as a *Droop-e* device compared to the other devices. Generator 4 delivers approximately 30% more power, while generator 8 delivers less power, as the control objective for devices near the maximum power is to limit the output.

The autonomous power sharing initiation times for *Droop-e* controlled devices 0, 4, and 8, occurred at 6.2, 5.5, and

4.7 seconds, respectively, as seen by the indicators in Fig. 11. Because the power sharing controller is activated by local measurements, the activation criteria is met at different times. The change in power output is a function of the local device deviation from the specified power sharing droop, and therefore a different power rate of change is expected for each *Droop-e* device. The novelty of the power sharing controller is such that despite distributed generation devices with disparate activation times and a variety in delivered transient power, all devices arrive at the target power sharing droop value autonomously, with zero communication.

VI. CONCLUSION

In future power systems dominated by renewable power generators, the presence of battery energy storage systems at a variety of dispatches will grow in prevalence. This paper presented the novel *Droop-e* control strategy for grid-forming power electronic converters that establishes a non-linear active power–frequency relationship based on an exponential function of the power output. The advantages of this control approach consist of an increased utilization of available headroom to mitigate frequency excursions and the rate of change of frequency, accompanied by a natural limiting behavior. An auxiliary controller achieves autonomous power sharing following the initial transient stabilization. The motivation and design of the *Droop-e* control was presented, and the stability of the controller was proven analytically, and with electromagnetic transient time-domain simulations. The simulations on a larger network established the autonomous, and superior, frequency stability of networks with *Droop-e* power-electronic converters. Potential directions for future research are identified as:

- Additional stability analyses, both analytical and large-signal, of larger networks with a more diverse set of frequency responsive devices.
- Optimality approaches for the tuning of the α and β parameters.
- Investigation of *Droop-e* devices at the interconnection level, where the larger headroom utility may achieve frequency response obligations with fewer devices.

REFERENCES

- [1] J. A. Taylor, S. V. Dhople, and D. S. Callaway, “Power systems without fuel,” *Renewable and Sustainable Energy Reviews*, vol. 57, pp. 1322–1336, 2016.
- [2] R. W. Kenyon, M. Bossart, M. Marković, K. Doubleday, R. Matsuda-Dunn, S. Mitova, S. A. Julien, E. T. Hale, and B.-M. Hodge, “Stability and control of power systems with high penetrations of inverter-based resources: An accessible review of current knowledge and open questions,” *Solar Energy*, 2020.
- [3] F. Milano, F. Dörfler, G. Hug, D. J. Hill, and G. Verbič, “Foundations and Challenges of Low-Inertia Systems,” in *2018 Power Systems Computation Conference (PSCC)*, Jun. 2018, pp. 1–25.
- [4] N. Hatziaargyriou, J. Milanovic, C. Rahmann, V. Ajjarapu, C. Canizares, I. Erlich, D. Hill, I. Hiskens, I. Kamwa, B. Pal, P. Pourbeik, J. Sanchez-Gasca, A. Stankovic, T. Van Cutsem, V. Vittal, and C. Vournas, “Definition and Classification of Power System Stability – Revisited & Extended,” *IEEE Transactions on Power Systems*, vol. 36, no. 4, pp. 3271–3281, Jul. 2021.
- [5] A. Ulbig, T. S. Borsche, and G. Andersson, “Impact of Low Rotational Inertia on Power System Stability and Operation,” *IFAC Proceedings Volumes*, vol. 47, no. 3, pp. 7290–7297, Jan. 2014.

- [6] Y. Cheng, L. Fan, J. Rose, S.-H. Huang, J. Schmall, X. Wang, X. Xie, J. Shair, J. R. Ramamurthy, N. Modi, C. Li, C. Wang, S. Shah, B. Pal, Z. Miao, A. Isaacs, J. Mahseredjian, and J. Zhou, "Real-World Subsynchronous Oscillation Events in Power Grids With High Penetrations of Inverter-Based Resources," *IEEE Transactions on Power Systems*, vol. 38, no. 1, pp. 316–330, Jan. 2023.
- [7] North American Electric Reliability Corporation, "Grid Forming Technology: Bulk Power System Reliability Considerations," North American Electric Reliability Corporation, Atlanta, GA, NERC Reliability Guideline, Dec. 2021.
- [8] A. Tayyebi, D. Groß, A. Anta, F. Kupzog, and F. Dörfler, "Frequency Stability of Synchronous Machines and Grid-Forming Power Converters," *IEEE Journal of Emerging and Selected Topics in Power Electronics*, vol. 8, no. 2, pp. 1004–1018, Jun. 2020.
- [9] E. A. S. Ducoin, Y. Gu, B. Chaudhuri, and T. C. Green, "Analytical Design of Contributions of Grid-Forming & Grid-Following Inverters to Frequency Stability," *IEEE Transactions on Power Systems*, pp. 1–14, 2024.
- [10] A. Sajadi, R. W. Kenyon, and B.-M. Hodge, "Synchronization in electric power networks with inherent heterogeneity up to 100% inverter-based renewable generation," *Nature Communications*, vol. 13, no. 1, p. 2490, May 2022.
- [11] R. W. Kenyon, A. Sajadi, M. Bossart, A. Hoke, and B.-M. Hodge, "Interactive Power to Frequency Dynamics Between Grid-Forming Inverters and Synchronous Generators in Power Electronics-Dominated Power Systems," *IEEE Systems Journal*, pp. 1–12, 2023.
- [12] J. Rocabert, A. Luna, F. Blaabjerg, and P. Rodríguez, "Control of Power Converters in AC Microgrids," *IEEE Transactions on Power Electronics*, vol. 27, no. 11, pp. 4734–4749, Nov. 2012.
- [13] W. Du, Z. Chen, K. P. Schneider, R. H. Lasseter, S. Pushpak, F. K. Tuffner, and S. Kundu, "A Comparative Study of Two Widely Used Grid-Forming Droop Controls on Microgrid Small Signal Stability," *IEEE Journal of Emerging and Selected Topics in Power Electronics*, pp. 1–1, 2019.
- [14] P. Unruh, M. Nuschke, P. Strauß, and F. Welck, "Overview on Grid-Forming Inverter Control Methods," *Energies*, vol. 13, no. 10, p. 2589, Jan. 2020.
- [15] P. Piagi and R. H. Lasseter, "Autonomous control of microgrids," in *2006 IEEE Power Engineering Society General Meeting*, Jun. 2006, p. 8.
- [16] H. Beck and R. Hesse, "Virtual Synchronous Machine," in *2007 9th International Conference on Electrical Power Quality and Utilisation*, Oct. 2007, pp. 1–6.
- [17] B. K. Poolla, D. Groß, and F. Dörfler, "Placement and Implementation of Grid-Forming and Grid-Following Virtual Inertia and Fast Frequency Response," *IEEE Transactions on Power Systems*, vol. 34, no. 4, pp. 3035–3046, Jul. 2019.
- [18] B. B. Johnson, M. Sinha, N. G. Ainsworth, F. Dörfler, and S. V. Dhople, "Synthesizing Virtual Oscillators to Control Islanded Inverters," *IEEE Transactions on Power Electronics*, vol. 31, no. 8, pp. 6002–6015, Aug. 2016.
- [19] U. B. Tayab, M. A. B. Roslan, L. J. Hwai, and M. Kashif, "A review of droop control techniques for microgrid," *Renewable and Sustainable Energy Reviews*, vol. 76, pp. 717–727, Sep. 2017.
- [20] Y. Jiang, A. Bernstein, P. Vorobev, and E. Mallada, "Grid-Forming Frequency Shaping Control for Low-Inertia Power Systems," in *2021 American Control Conference (ACC)*, May 2021, pp. 4184–4189, iSSN: 2378-5861.
- [21] L. Huang, H. Xin, Z. Wang, K. Wu, H. Wang, J. Hu, and C. Lu, "A Virtual Synchronous Control for Voltage-Source Converters Utilizing Dynamics of DC-Link Capacitor to Realize Self-Synchronization," *IEEE Journal of Emerging and Selected Topics in Power Electronics*, vol. 5, no. 4, pp. 1565–1577, Dec. 2017.
- [22] R. H. Lasseter, Z. Chen, and D. Pattabiraman, "Grid-Forming Inverters: A Critical Asset for the Power Grid," *IEEE Journal of Emerging and Selected Topics in Power Electronics*, vol. 8, no. 2, pp. 925–935, Jun. 2020.
- [23] R. Wang, Q. Sun, Y. Gui, and D. Ma, "Exponential-function-based droop control for islanded microgrids," *Journal of Modern Power Systems and Clean Energy*, vol. 7, no. 4, pp. 899–912, Jul. 2019.
- [24] Q. Zhong, "Robust Droop Controller for Accurate Proportional Load Sharing Among Inverters Operated in Parallel," *IEEE Transactions on Industrial Electronics*, vol. 60, no. 4, pp. 1281–1290, 2013.
- [25] D. Pattabiraman, R. H. Lasseter., and T. M. Jahns, "Comparison of Grid Following and Grid Forming Control for a High Inverter Penetration Power System," in *2018 IEEE Power Energy Society General Meeting (PESGM)*, Aug. 2018, pp. 1–5, iSSN: 1944-9933.
- [26] F. Conte, S. Massucco, G.-P. Schiapparelli, and F. Silvestro, "Day-Ahead and Intra-Day Planning of Integrated BESS-PV Systems Providing Frequency Regulation," *IEEE Transactions on Sustainable Energy*, vol. 11, no. 3, pp. 1797–1806, Jul. 2020.
- [27] R. W. Kenyon, A. Sajadi, A. Hoke, and B.-M. Hodge, "Using a Grid-Forming Inverter to Stabilize a Low-Inertia Power System – Maui Hawaiian Island," in *2022 IEEE PES Innovative Smart Grid Technologies Conference Europe (ISGT-Europe)*, Oct. 2022, pp. 1–6.
- [28] P. W. Sauer, M. A. Pai, and Chow, J. H., *Power System Dynamics and Stability: With Synchrophasor Measurement and Power System Toolbox*, 2nd ed. Wiley-IEEE Press, 2017.
- [29] R. W. Kenyon, A. Sajadi, A. Hoke, and B.-M. Hodge, "Open-Source PSCAD-Grid-Following and Grid-Forming Inverters and A Benchmark for Zero-Inertia Power System Simulations," in *2021 IEEE Kansas Power and Energy Conference (KPEC)*, Apr. 2021, pp. 1–6.
- [30] U. Markovic, O. Stanojevic, P. Aristidou, E. Vrettos, D. S. Callaway, and G. Hug, "Understanding Small-Signal Stability of Low-Inertia Systems," *IEEE Transactions on Power Systems*, pp. 1–1, 2021.
- [31] L. Xiong, X. Liu, Y. Liu, and F. Zhuo, "Modeling and stability issues of voltage-source converter dominated power systems: A review," *CSEE Journal of Power and Energy Systems*, pp. 1–18, 2020.
- [32] Manitoba Hydro International Ltd, "Power Systems Computer Aided Design." [Online]. Available: <https://www.mhi.ca/products/pscad>
- [33] R. W. Kenyon, "PyPSCAD." Golden, CO, Nov. 2020. [Online]. Available: <https://github.com/NREL/PyPSCAD>
- [34] T. Sarkar and O. Pereira, "Using the matrix pencil method to estimate the parameters of a sum of complex exponentials," *IEEE Antennas and Propagation Magazine*, vol. 37, no. 1, pp. 48–55, Feb. 1995.
- [35] Manitoba Hydro International Ltd, "PSCAD: IEEE 39 Bus System." [Online]. Available: <https://www.pscad.com/knowledge-base/article/28>

VII. APPENDIX

Tables V and VI provide the detailed device and system parameters, and the dispatch of the 39-bus simulation cases, respectively.

TABLE V: Device and Network Parameters

Parameter	Value	Par...	Value	Par...	Value
$H(sec)$	3.01	$X_d(pu)$	1.3125	$X'_d(pu)$	0.1813
X_q	1.2578	$X'_q(pu)$	0.25	$T'_{do}(sec)$	5.89
$T'_{qo}(sec)$	0.6	K_A	20	$T_A(sec)$	0.2
K_E	1.0	$T_E(sec)$	0.314	K_F	0.063
$T_F(sec)$	0.35	$S_E - \gamma$	0.0039	$S_E - \epsilon$	1.555
$M_D(\%)$	5	$\omega_B(rad/s)$	377	$X_a(pu)$	0.05
$X_b(pu)$	0.05	$D_I - \alpha$	0.002	$D_I - \beta$	3.0
$X_{GFM}(pu)$	0.15	$R_{GFM}(pu)$	0.005	$T_{fil}(sec)$	0.0167
$P_2(pu)$	0.75	$Q_2(pu)$	0.25	$V_1(pu)$	1.02
$V_3(pu)$	1.02	$S_G(MVA)$	100	$S_I(MVA)$	50
$L_f(pu)$	0.15	$R_f(pu)$	0.005	$C_f(pu)$	2.5
$R_{cap}(pu)$	0.005	k_C^i	1.19	k_C^p	0.73
G_C	1.0	k_V^i	1.16	k_V^p	0.52
G_V	1.0				

TABLE VI: IEEE 39-Bus Configuration and Results

Generator	P (MW)	Generator Type for Case		
		39-A	39-B	39-C
0	250	SG	Linear-5%	<i>Droop-e</i>
1	678	SG	SG	SG
2	650	SG	SG	SG
3	632	SG	SG	SG
4	508	SG	Linear-5%	<i>Droop-e</i>
5	650	SG	SG	SG
6	560	SG	SG	SG
7	540	SG	SG	SG
8	830	SG	Linear-5%	<i>Droop-e</i>
9	1000	SG	SG	SG